# Synthesis YFeO$_3$ by salt-assisted solution combustion method and its photocatalytic activity

**Yuanyuan CHEN, Jun YANG,**[†] **Xuelei WANG, Feiyi FENG, Yuanming ZHANG and Yu TANG**

**Department of Chemistry, Jinan University, Guangzhou 510632, People's Republic of China**

Single-crystalline YFeO$_3$ particles with the perovskite structure have been fabricated through a facile KCl-assisted solution combustion synthesis (SSCS) method, using alanine as a fuel and corresponding nitrates as oxidants. The effects of the fuel-to-nitrate ion (F/N) and the KCl-to-metal ratios (KCl/M) on the phase and microstructure of the products are studied in detail by X-ray diffraction analysis, scanning electron microscopy, low temperature N$_2$ adsorption, UV–visible diffuse reflection spectroscopy. It is remarkable that the introduction of KCl into the solution combustion synthesis (SCS) process results in a dramatic increase in surface of the obtained YFeO$_3$, i.e. a more than sixth-fold increase from 2.9 to 19.6 m$^2$/g when F/N = 0.30 and forty-fourth-fold increase from 0.5 to 24.2 m$^2$/g in the case of F/N = 0.33. Results show that both of YFeO$_3$ nanoparticles prepared by SCS and SSCS exhibit excellent photocatalytic activity for the photodegradation of rhodamine B in the presence of H$_2$O$_2$. The photo-generated holes (h$^+$) and •OH were the main active species of YFeO$_3$ for RhB degradation under visible light irradiation.

## 1. Introduction

Recently, perovskite ABO$_3$ series nanomaterials, one of the most attractive and interesting mixed oxides, have been used as functional material in many fields due to their unique physico-chemical properties, such as unique electrical, magnetic and catalytic properties.[1)–3)] Yttrium orthoferrite (YFeO$_3$), which has a distorted perovskite structure,[4)–6)] has been widely studied for its magnetic and magneto-optical properties and used in gas sensors, environmental monitoring applications and catalysis.[7)] YFeO$_3$-based catalysts have been explored for photocatalytic oxidation of organic dyes and exhibit higher visible-light photocatalytic activity than TiO$_2$ (P$_{25}$).[8)–10)] Furthermore, YFeO$_3$ has been found to be ferromagnetic, which renders a possibility for recovery of YFeO$_3$ with an external magnet in practical applications.[6)] Up to now, various approaches have been applied to fabricate perovskite YFeO$_3$, such as combustion synthesis, sol–gel, co-precipitation, thermal decomposition, microwave-assisted and solid state routes.[10)–15)] Most of the current approaches for synthesis of single phase perovskite YFeO$_3$ require the calcination process at high temperature, which leads to high energy-consumption and the growth of large size particles. Furthermore, perovskite YFeO$_3$ is thermodynamically unstable and can transform to thermo-dynamically stable Fe$_3$O$_4$ or Y$_3$Fe$_5$O$_{12}$ at high temperature, which makes the phase-selective synthesis of pure perovskite YFeO$_3$ a difficult task.[3)]

Among the various synthetic routes, solution combustion synthesis has been regarded as one of effective and economic approaches owing to its convenient processing, simple experimental setup, significant saving in time and energy and homogeneous products.[16),17)] However, conventional solution combustion synthesis (SCS) of well-dispersed nanocrystalline oxide particles faces two difficulties of inhibiting particulate agglomeration and promoting phase formation. Considering the situation, many attempts have been made to prevent resultant particles from agglomerating and sintering by choosing fuel and adjusting fuel-to-oxidant molar ratio.[18)] In many cases, the nanophase rather than nano-sized particles were obtained through a solution combustion synthesis route.[19),20)] Therefore, controlled synthesis of nanostructures via solution combustion route surely has been an experimental challenge. Herein, we employed a salt-assisted solution combustion synthesis (SSCS) to prepare YFeO$_3$ nano-particles using alanine as a fuel and corresponding metal nitrates as oxidants. Effect of the fuel-to-oxidant and the salt-to-metal ratios on the composition, structure and properties of the products is studied in detail.

## 2. Experimental

All reagents were of analytical grade and used without further purification. In a typical synthesis, 3.5 mmol of Y(NO$_3$)$_3$·6H$_2$O and 3.5 mmol of Fe(NO$_3$)$_3$·9H$_2$O were dissolved in 8 ml deion-ized water. According to the required molar ratios of alanine to nitrate (F/N) and KCl to total metal ions (KCl/M), proper amounts of L-$\alpha$ alanine (Ala, C$_3$H$_7$NO$_2$) and KCl was added to the mixture solution under magnetic stirring. After the resultant solution became a brown homogeneous solution, it was trans-ferred into a ceramic crucible and then placed in a muffle furnace at 573 K. The solution bubbled up and auto-1ighted with the rapid evolution of a large volume of gases. In order to remove salt, the as-synthesized powder was boiled in deionized water, filtered and washed several times with deionized water and ethanol. Finally, the product was dried in an oven at 353 K (S-YFeO$_3$). For comparison, YFeO$_3$ nanoparticles (C-YFeO$_3$) were prepared by the conventional solution combustion synthesis (SCS) without KCl addition.

The crystalline phases of the samples were identified by X-ray diffraction (MSAL XD-2) with a graphite monochromator and

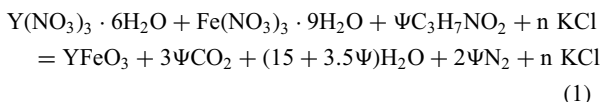† Corresponding author: J. Yang; E-mail: tyangj@jnu.edu.cn or tyangj@126.com

Cu K$\alpha$1 ($\lambda = 0.15405$ nm) radiation. The crystallite size was determined based on the XRD patterns using the Sherrer's equation: $D = 0.89\lambda/(\beta \cos\theta)$. The morphologies were observed with a scanning electron microscope (JEOL JSM1-6330F, Japan). The specific surface areas of the samples were measured by using $N_2$ adsorption at 77 K (Tristar 3000). The diffuse reflectance UV–vis spectra of the samples were recorded using a varian (Cary 5000) spectrophotometer equipped with an integrating sphere accessory. Barium sulphate was used as reference for the reflectance spectra.

The photoactivity was evaluated by the photodegradation of rhodamine B (RhB) in aqueous solution. A 175 W metal halide lamp was used as the light source. To limit the irradiation wavelength, the light beam was passed through a filter to cutoff wavelengths shorter than 420 nm. The initial concentration of RhB in a glass reaction vessel was fixed at 10 mg/L and the photocatalyst loading was 1 g/L. Prior to illumination, the suspension was magnetically stirred in the dark for 30 min to establish the adsorption–desorption equilibrium and then 0.3 ml of 30% hydrogen peroxide solution was added. During irradiation, stirring was maintained to keep the mixture in suspension. At regular intervals, samples were taken from the suspension. The liquid was analyzed by UV–visible spectrophotometer (TU1801, PGENERAL) after the solid photocatalyst was removed by centrifuge.

## 3. Results and discussion

### 3.1 XRD and BET analyses of YFeO$_3$ nanoparticles

Solution combustion synthesis is based on the intense redox reaction between oxidant and reductant, which releases large amount of heat in an instant and results in a drastic temperature increase of the reaction system (1000–1600°C), yielding the product with specific phase and morphology. According to the principle of propellant chemistry,[21] it is assumed that in the case of alanine–nitrate combustion, primarily $N_2$, $CO_2$ and $H_2O$ are evolved as the gaseous products. The salt-assisted redox combustion reaction can be generalized and expressed as follows:

$$Y(NO_3)_3 \cdot 6H_2O + Fe(NO_3)_3 \cdot 9H_2O + \Psi C_3H_7NO_2 + n\,KCl$$
$$= YFeO_3 + 3\Psi CO_2 + (15 + 3.5\Psi)H_2O + 2\Psi N_2 + n\,KCl$$
$$\tag{1}$$

In this work, a series control experiments, including fuel-to-oxidant molar ratio (F/N) and amount of added salt, were carried out to investigate the effect of F/N and KCl/M ratios on characteristics of the as-synthesized powders systematically. Results reveal that the auto-propagating combustion reaction occurs for a limited range of F/N ratio, depending on the nature of the fuel and the amount of the added salt.[22]

**Figure 1** shows the XRD patterns of the samples prepared at different F/N ratios by combustion synthesis whether it exists salt or not. It can be clearly seen that the auto-propagating combustion reaction ceases to occur if either F/N ratio is below 0.1 in the absence of salt [Fig. 1(A)] or F/N ratio is below 0.23 in the presence of salt [Fig. 1(B)]. As is shown in Fig. 1(A), a single phase of YFeO$_3$ with perovskite structure is formed in the F/N ratio range of 0.17 to 0.37. The peaks can be assigned to (111), (200), (121), (002), (202), (301) and (123) plane of perovskite structure YFeO$_3$ (JCPDS: 39-1489). However, in the case of SSCS route [Fig. 1(B)], the resultants present the amorphous phase when the F/N is below 0.23 with KCl/M = 1:2. It may occur because of the temperature decreasing, which is agreement with the theoretical analysis. It is thought that salt
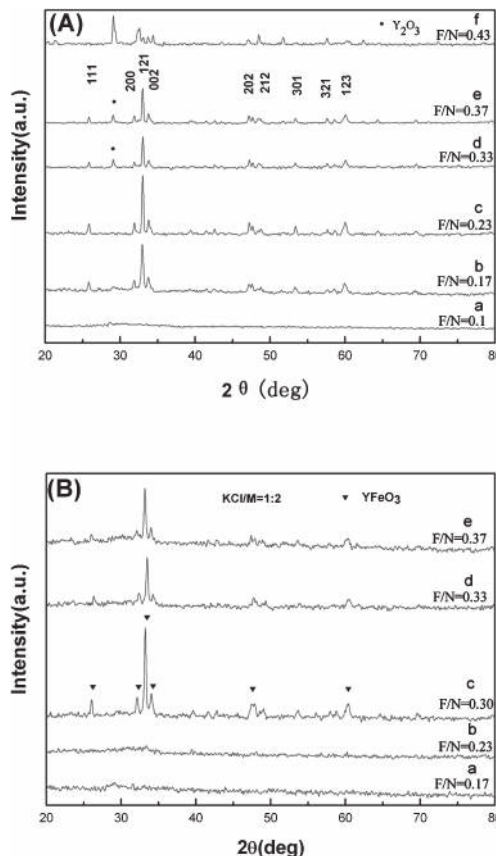


Fig. 1. XRD patterns of samples prepared at different fuel-to-oxidant (F/N) ratios (A) in the absence of salt: (a) F/N = 0.10 fuel-lean (−70%), (b) F/N = 0.17 fuel-lean (−50%), (c) F/N = 0.23 fuel-lean (−30%), (d) F/N = 0.33 (stoichiometric), (e) F/N = 0.37 fuel-rich (+10%), (f) F/N = 0.43 fuel-rich (+30%); (B) in the presence of salt (KCl/M = 1/2):(a) F/N = 0.17 (−50%), (b) F/N = 0.23 (−30%), (c) F/N = 0.30 (−10%), (d) F/N = 0.33 (stoichiometric), (e) F/N = 0.37 (+10%).

adsorbs large reaction heat due to the temperature rising and melting of the added salt in the combustion synthesis process.[23] Furthermore, with the increasing F/N to 0.3, perovskite YFeO$_3$ appears and its diffraction peaks become narrower and stronger.

**Figure 2** shows XRD patterns of YFeO$_3$ prepared by SSCS as a function of the amount of KCl. In the case of F/N = 0.3, YFeO$_3$ with perovskite structure is formed in the KCl/M ratio range of 0 to 2/3, whereas the resultants present the amorphous phase when KCl/M = 1. However, in the case of F/N = 0.33, a single phase of YFeO$_3$ with perovskite structure is formed in the KCl/M ratio range of 0 to 1, not in the case of KCl/M = 3:2. These indicated that only the right amount of KCl could form target product in the case of equal F/N ratio.

**Table 1** summarizes the effect of the added amount of KCl on the properties of YFeO$_3$ prepared via the SSCS process. It is remarkable that the introduction of KCl into the SCS process results in a dramatic increase in surface area of the obtained YFeO$_3$, i.e. a more than sixth-fold increase from 2.9 to 19.6 m$^2$/g when F/N = 0.3 and forty-fourth-fold increase from 0.5 to 24.2 m$^2$/g in the case of F/N = 0.33. However, under the condition of the same F/N ratio, further increasing KCl/M leads to a decrease in surface area and the possible formation of amorphous phase (Fig. 2), which reveals that the auto-propagating combustion reaction occurs for a limited range of KCl/M ratio.
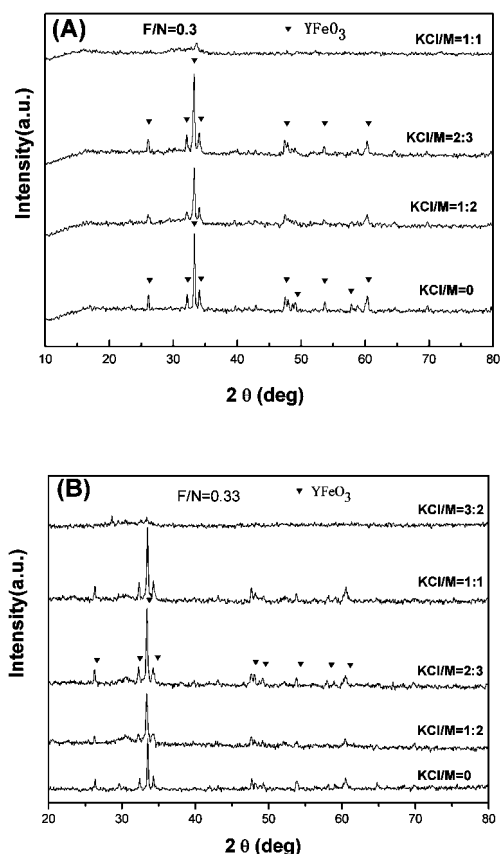
Fig. 2. XRD pattern evolution for the YFeO₃ samples as a function of KCl/M: (A) F/N = 0.3 and (B) F/N = 0.33.

Table 1. The textural properties of samples synthesized with different amount of salt

| F/N (molar ratio) | KCl/M (molar ratio) | Phase structure | BET special surface area ($m^2/g$) | Crystallite size (nm) |
|---|---|---|---|---|
| 0.30 | 0 | orthorhombic | 2.9 | 24 |
| 0.30 | 1/2 | orthorhombic | 19.6 | 21 |
| 0.30 | 2/3 | orthorhombic | 15.8 | 25 |
| 0.30 | 1 | amorphous | — | — |
| 0.33 | 0 | orthorhombic | 0.5 | 30 |
| 0.33 | 1/2 | orthorhombic | 24.2 | 22 |
| 0.33 | 2/3 | orthorhombic | 18.9 | 27 |
| 0.33 | 1 | orthorhombic | 10.4 | 28 |

## 3.2 SEM of YFeO₃ nanoparticles

The morphologies of the resultants can be affected by adding different amount of salt besides by altering F/N molar ratio, which was demonstrated by SEM. As is shown in Fig. 3, these images reveal remarkable changes in microstructures, including grain size, porosity and particle distribution by changing KCl/M molar ratio. **Figure 3**(a) and 3(b) exhibit the typical morphology of the YFeO₃ particles obtained in the SCS route, foamy agglomerated particles with a wide distribution and presence of large voids in its structure. The formation of these features is attributed to the large volume of gas evolved during combustion. It is obvious that the introduction of salt (KCl) into the redox mixture solution breaks up its agglomerated structure and leads to a great improvement in dispersing state and an obvious reduction in particle size,[17),24)] which agrees well with the results of low temperature N₂ adsorption experiments (Table 1).

## 3.3 UV–vis diffuse reflection spectra of YFeO₃ nanoparticles

**Figure 4** shows the diffuse reflection spectra of TiO₂, YFeO₃ prepared by SCS and SSCS (KCl/M = 1/2). It can be seen that the TiO₂ [Fig. 4(e)] only presents a strong reflectance in UV region, while single phase YFeO₃ nanoparticles can absorb the visible light, which makes it the potential visible-light-driven photocatalyst (Fig. 4). With the addition of KCl, as-synthesized YFeO₃ results in a slight decrease of the absorption in the visible range in comparison with that of no KCl addition.
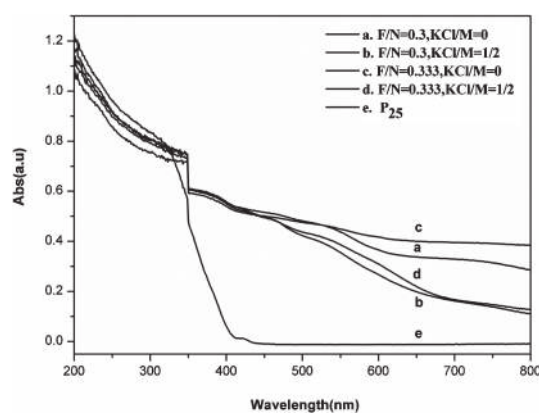


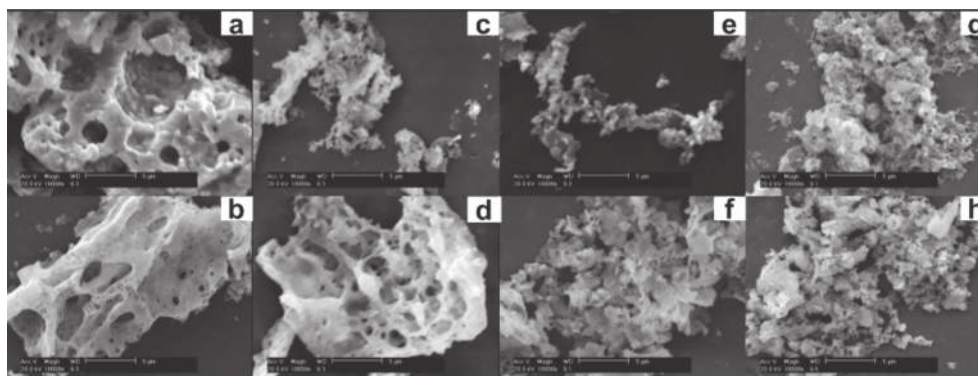Fig. 4. UV–vis diffuse reflection spectra of YFeO₃ prepared by SSCS process and TiO₂.



Fig. 3. SEM micrographs of YFeO₃ nanoparticles prepared by combustion synthesis: (a) KCl/M = 0, F/N = 0.3; (b) KCl/M = 0, F/N = 0.33; (c) KCl/M = 1:2, F/N = 0.3; (d) KCl/M = 1:2, F/N = 0.33; (e) KCl/M = 2:3, F/N = 0.3; (f) KCl/M = 2:3, F/N = 0.33; (g) KCl/M = 1:1, F/N = 0.3; (h) KCl/M = 1:1, F/N = 0.33.
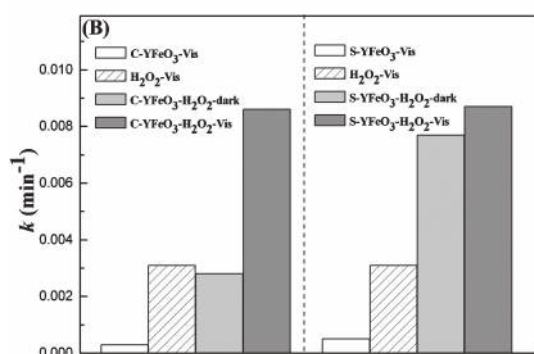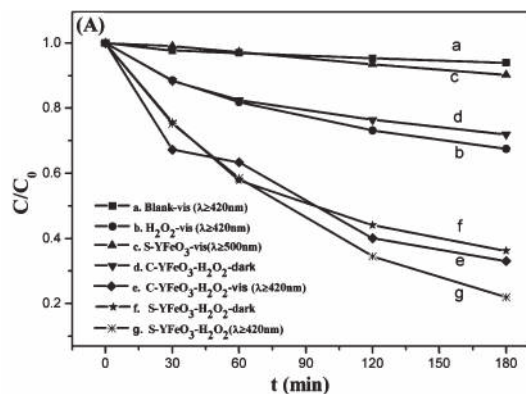
Fig. 5. (A) Degradation of RhB (10 mg/L) over C-YFeO$_3$ and S-YFeO$_3$ catalysts; (B) RhB degradation rate constants under different reaction conditions.
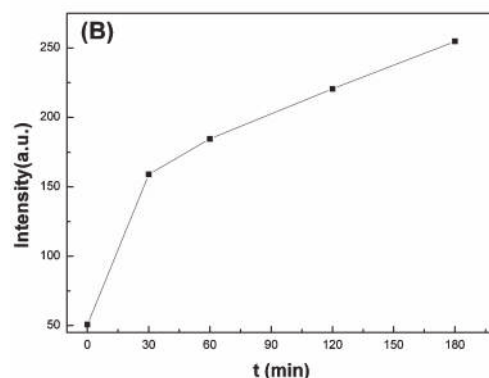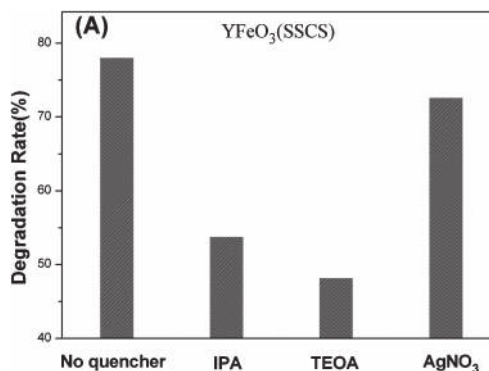


Fig. 6. (A) Trapping experiment of active species during the photocatalytic reaction under visible light irradiation; (B) fluorescent intensity of TAOH under visible light irradiation.

### 3.4 Photocatalystic activity and Photocatalytic mechanism

In this work, photocatalytic degradation of RhB solution under visible light irradiation ($\lambda > 420$ nm) was examined with the orthorhombic YFeO$_3$ prepared by SSCS and SCS, results were shown in **Fig. 5**(A). It can be seen that RhB is hardly degraded in the absence of photocatalyst (curve a). The degradation ratio of RhB is obviously enhanced for nanoparticles YFeO$_3$ in the presence of H$_2$O$_2$ under visible light irradiation. In the control experiment, RhB is slightly degraded in the presence of hydrogen peroxide under visible light irradiation (curve b). Curves e and g show that S-YFeO$_3$ exhibits much higher photoactivity than C-YFeO$_3$ in the presence of H$_2$O$_2$, because of its increased surface area and reduced particle size. Catalyst surface area and particle size play an important role in the photocatalytic activity, since the predominant way of electron–hole recombination may be different depending on the particle size and surface area.[25] In order to explore the influence of the excitation of RhB on the photodegradation process, the photoactivity of YFeO$_3$ for RhB degradation under visiblelight irradiation ($\lambda \geq 500$ nm) was carried out.[26]–[28] It can be found that only 9.8% RhB was photodegraded, indicating that the excitation of RhB has a slight effect on the photocatalytic process (curve c).

It is agreed upon that the initial concentration of organic pollutants on the photodegradation rate can be described well by Langmuir Hinshewood kinetic model, which has been widely used in liquid- and gas-phase photocatalysis.[1] In the integrated form of: $kt = \ln C_0/C$, where $C_0$ is the initial concentration of RhB solution, $k$ represents apparent rate constant, t is reaction time, and

the $k$ values under different reaction conditions are compared in Fig. 5(B). It can be seen that either YFeO$_3$ or H$_2$O$_2$ alone provides very weak degradation ability under visible light irradiation, while YFeO$_3$ behaves as a good photocatalyst for the degradation of RhB in the presence of H$_2$O$_2$. The $k$ value of C-YFeO$_3$ and S-YFeO$_3$ in the presence of H$_2$O$_2$ under visible light irradiation is higher than that of YFeO$_3$–H$_2$O$_2$-dark system. This confirms that the introduction of visible light can provide an alternative approach to enhance the catalytic ability of YFeO$_3$ nanoparticles for the degradation of RhB in the presence of H$_2$O$_2$, which means that it's a photo-Fenton-like photocatalyst system.[29]–[32]

Although the detailed mechanism of photocatalysis varies with different pollutants, we have tried to analysis the main active species in this photocatalytic system. In order to detect the main active species during the photodegradation process of RhB, additional examinations were carried out via dissolving different trapping agents, such as IPA (a quencher of •OH), TEOA (a quencher of h$^+$) and AgNO$_3$ (a quencher of e$^-$), respectively, in the reaction solution before light irradiations.[28],[33],[34] **Figure 6**(A) displays the trapping experiment of active species during the photocatalytic degradation of RhB on S-YFeO$_3$ under visible light irradiation. It can be found that the addition of 1 mM AgNO$_3$ (a quencher of e$^-$) had a negligible effect on the degradation rate of RhB compared with no scavenger under otherwise identical conditions, indicating that e$^-$ was not the main reactive species. On the contrary, the photocatalytic degradation of RhB decreased significantly, with the addition of 1 mM TEOAor 1 mM IPA. Therefore, it can be concluded that photogenerated holes (h$^+$) and •OH are the main active species of YFeO$_3$ for RhB degradation
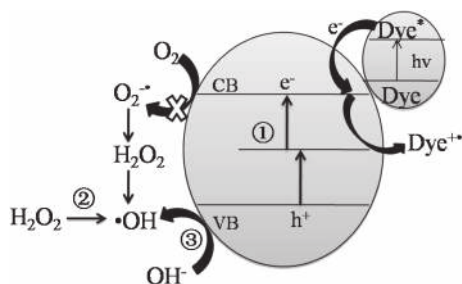
Fig. 7. Main processes occurring on YFeO₃ photocatalyst during the photodegradation of RhB.

under visible light irradiation. Figure 6(B) shows the fluorescent intensity of TAOH (quantification experiments of •OH production) under visible light irradiation during the photocatalytic reaction. With the extension of time, the fluorescent intensity of TAOH gradually increases, which demonstrates the production of the hydroxyl from the holes or electrons.[35] On the base of above results, the possible photocatalytic mechanism could be deduced as follows (**Fig. 7**): under visible light irradiation, photogenerated electron–hole pairs are formed in YFeO₃ nanoparticles under visible light irradiation (path ①). And the photo-Fenton reactions with $H_2O_2$ by the iron species generate •OH radicals and $OH^-$ (path ②). The leaving holes can also accept an electron from the hydroxyl group and there of more •OH radicals are generated (path ③). This means that both photogenerated holes and photo-Fenton-like process can lead to the formation of •OH radicals, which can then degrade RhB more efficiently.

## 4. Conclusions

The single-crystalline perovskite nanoparticles of YFeO₃ have been successfully prepared via a facile salt-assisted solution combusion method. The grain crystalline sizes of the prepared samples are found to be 20 to 30 nm. In the SSCS process, the instant salt precipitation in situ inhibits the formation of hard agglomerates and results in drastic increase in surface area. This procedure was suitable for the synthesis of well-dispersed YFeO₃ nanoparticles and could be potentially applied to the preparation of other perovskite nanoparticles. The degradation of RhB in water under visible light irradiation shows that perovskite YFeO₃ nanoparticles have excellent photocatalytic properties in the presence of $H_2O_2$. The photo-generated holes ($h^+$) and •OH were determined the main active species of YFeO₃ for RhB degradation under visible light irradiation.

## References

1) J. Yang, X. C. Li, J. Y. Zhou, Y. Tang, Y. M. Zhang and Y. W. Li, *J. Alloys Compd.*, **509**, 9271–9277 (2011).
2) D. S. Schmool, N. Keller, M. Guyot, R. Krishnan and M. Tessier, *J. Magn. Magn. Mater.*, **195**, 291–298 (1999).
3) S. Mathur, M. Veith, R. Rapalaviciute, H. Shen, G. F. Goya, W. L. Martins Filho and T. S. Berquo, *Chem. Mater.*, **16**, 1906–1913 (2004).
4) J. Li, U. G. Singh, T. D. Schladt, J. K. Stalick, S. L. Scott and R. Seshadri, *Chem. Mater.*, **20**, 6567–6576 (2008).
5) R. Maiti, S. Basu and D. Chakravorty, *J. Magn. Magn. Mater.*, **321**, 3274–3277 (2009).
6) P. Tang, H. Chen, F. Cao and G. X. Pan, *Catal. Sci.Technol.*, **1**, 1145–1148 (2011).
7) H. Shen, J. Xu, A. Wu, J. Zhao and M. Shi, *Mater. Sci. Eng., B*, **157**, 77–80 (2009).
8) X. M. Lu, J. M. Xie, H. M. Shu, J. Liu, C. Q. Yin and J. M. Lin, *Mater. Sci. Eng., B*, **138**, 289–292 (2007).
9) W. C. Wang, S. Li, Y. Y. Wen, M. C. Gong, L. Zhang, Y. L. Yao and Y. Q. Chen, *Acta. Phys-Chim. Sin.*, **24**, 1761–1766 (2008).
10) Y. W. Zhang, J. X. Yang, J. F. Xu, Q. Y. Gao and Z. L. Hong, *Mater. Lett.*, **81**, 1–4 (2012).
11) L. Wu, J. C. Yu, L. Z. Zhang, X. C. Wang and S. K. Li, *J. Solid State Chem.*, **177**, 3666–3674 (2004).
12) M. M. Rashad, M. M. Hessien, A. EI-Midany and I. A. Ibrahim, *J. Magn. Magn. Mater.*, **32**, 3752–3757 (2009).
13) N. A. Tien, O. V. Almjasheva, I. Y. Mittova, O. V. Stognei and S. A. Soldatenko, *Inorg. Mater.*, **45**, 1304–1308 (2009).
14) V. Berbenni, C. Milanese, G. Bruni, A. Girella and A. Marini, *Thermochim. Acta*, **521**, 218–223 (2011).
15) H. Shen, J. Y. Xu and A. H. Wu, *J. Rare Earths*, **28**, 416–419 (2010).
16) K. C. Patil, S. T. Aruna and T. Mimani, *Curr. Opin. Solid State Mater. Sci.*, **6**, 507–512 (2002).
17) J. Yang, X. C. Li, X. Z. Deng, Z. D. Huang and Y. M. Zhang, *J. Ceram. Soc. Japan*, **120**, 579–583 (2012).
18) R. K. Lenka, T. Mahata, P. K. Sinha and A. K. Tyagi, *J. Alloys Compd.*, **466**, 326–329 (2008).
19) C. H. Yan, Z. G. Xu, F. X. Cheng, Z. M. Wang, L. D. Sun, C. S. Liao and J. T. Jia, *Solid State Commun.*, **111**, 287–291 (1999).
20) M. B. Kakade, S. Ramanathan and P. V. Ravindran, *J. Alloys Compd.*, **350**, 123–129 (2003).
21) S. R. Jain, K. C. Adiga and V. R. P. Vemeker, *Combust. Flame*, **40**, 71–79 (1981).
22) W. F. Chen, F. S. Li, J. Y. Yu and L. L. Liu, *Mater. Res. Bull.*, **41**, 2318–2324 (2006).
23) W. F. Chen, F. S. Li, J. Y. Yu and L. L. Liu, *Mater. Sci. Eng., B*, **133**, 151–156 (2006).
24) M. Lackner, Combustion Synthesis: Novel Routes to Novel Materials. *Bentham Science Publishers* (2010) pp. 141–148.
25) O. Carp, C. L. Huisman and A. Reller, *Prog. Solid State Chem.*, **32**, 33–177 (2004).
26) X. Yan, T. Ohno, K. Nishilima, R. Abe and B. Ohtani, *Chem. Phys. Lett.*, **429**, 606–610 (2006).
27) M. Mrowetz, W. Balcerski, A. J. Colussi and M. R. Hoffmann, *J. Phys. Chem. B*, **108**, 17269–17273 (2004).
28) L. Q. Ye, J. Y. Liu, Z. Jiang, T. Y. Peng and L. Zan, *Appl. Catal., B: Environ*, **142–143**, 1–7 (2013).
29) L. Ju, Z. Chen, L. Fang, W. Dong, F. Zheng and M. Shen, *J. Am. Ceram. Soc.*, **94**, 3418–3424 (2011).
30) S. Tian, J. Zhang, J. Chen, L. Kong, J. Lu, F. Ding and Y. Xiong, *Ind. Eng. Chem. Res.*, **52**, 13333–13341 (2013).
31) R. Jusoh, A. A. Jalil, S. Triwahyono, A. Idris, S. Harona, N. Sapawe, N. F. Jaafar and N. W. C. Jusoh, *Appl. Catal., A: Gen.*, **469**, 33–44 (2014).
32) J. An, L. Zhu, Y. Zhang and H. Tang, *J. Environ. Sci.*, **25**, 1213–1225 (2013).
33) Y. N. Huo, J. Zhang, M. Miao and Y. Jin, *Appl. Catal., B: Environ.*, **111–112**, 334–341 (2012).
34) Y. Wang, K. J. Deng and L. Z. Zhang, *J. Phys. Chem. C*, **115**, 14300–14308 (2011).
35) H. Cheng, B. Huang, Y. Dai, X. Qin and X. Zhang, *Langmuir*, **26**, 6618–6624 (2010).